

Tests of stellar model atmospheres by optical interferometry

VLTI/VINCI limb-darkening measurements of the M4 giant ψ Phe^{*}

M. Wittkowski¹, J. P. Aufdenberg², and P. Kervella³

¹ European Southern Observatory, Karl-Schwarzschild-Str. 2, 85748 Garching bei München, Germany
e-mail: mwittkow@eso.org

² Harvard-Smithsonian Center for Astrophysics, 60 Garden Street, Mail Stop 15, Cambridge, MA 02138, USA
e-mail: jaufdenberg@cfa.harvard.edu

³ European Southern Observatory, Casilla 19001, Santiago 19, Chile; e-mail: pkervell@eso.org

Received ...; accepted ...

Abstract. We present K -band interferometric measurements of the limb-darkened (LD) intensity profile of the M4 giant star ψ Phoenicis obtained with the Very Large Telescope Interferometer (VLTI) and its commissioning instrument VINCI. High-precision squared visibility amplitudes in the second lobe of the visibility function were obtained employing two 8.2 m Unit Telescopes (UTs). This succeeded one month after light from UTs was first combined for interferometric fringes. In addition, we sampled the visibility function at small spatial frequencies using the 40 cm test siderostats. Our measurement constrains the diameter of the star as well as its center-to-limb intensity variation (CLV). We construct a spherical hydrostatic PHOENIX model atmosphere based on spectrophotometric data from the literature and confront its CLV prediction with our interferometric measurement. We compare as well CLV predictions by plane-parallel hydrostatic PHOENIX, ATLAS 9, and ATLAS 12 models. We find that the Rosseland angular diameter as predicted by comparison of the spherical PHOENIX model with spectrophotometry is in good agreement with our interferometric diameter measurement. The shape of our measured visibility function in the second lobe is consistent with all considered PHOENIX and ATLAS model predictions, and significantly different from uniform disk (UD) and fully darkened disk (FDD) models. We derive high-precision fundamental parameters for ψ Phe, namely a Rosseland angular diameter of 8.13 ± 0.2 mas, with the Hipparcos parallax corresponding to a Rosseland linear radius R of $86 \pm 3 R_{\odot}$, and an effective temperature of 3550 ± 50 K, with R corresponding to a luminosity of $\log L/L_{\odot} = 3.02 \pm 0.06$. Together with evolutionary models, these values are consistent with a mass of $1.3 \pm 0.2 M_{\odot}$, and a surface gravity of $\log g = 0.68 \pm 0.11$.

Key words. Techniques: interferometric – Stars: atmospheres – Stars: fundamental parameters – Stars: late-type – Stars: individual: ψ Phe

1. Introduction

Stellar atmosphere models predict the spectrum emerging from every point of a stellar disk. However, model atmospheres are usually only constrained by comparison to integrated stellar spectra. Optical interferometry has proven its capability to go beyond this principal test of the predicted flux, and to probe the wavelength-dependent center-to-limb intensity variation (CLV) across the stellar disk. In addition, the measurement of the stellar angular diameter together with the bolometric flux is the primary measure of the effective temperature, one of the most im-

portant parameters for modeling stellar atmospheres and stellar evolution.

Further tests of stellar atmosphere models by interferometric observations help to improve the reliability of results in all areas of astrophysics where such models are used. Cool giants and AGB stars are of interest for atmosphere modeling since they allow the study of extended stellar atmospheres and the stellar mass-loss process. Red giants are also used as probes of the chemical enrichment history of nearby galaxies through detailed abundance measurements of the Calcium infrared triplet which rely on model atmospheres.

However, the required direct measurements of stellar intensity profiles are among the most challenging programs in modern optical interferometry. Since more than one resolution element across the stellar disk is needed to determine surface structure parameters beyond diameters, the long baselines needed to obtain this resolution also produce very low visibility amplitudes corresponding to vanishing fringe con-

Send offprint requests to: M. Wittkowski, e-mail: mwittkow@eso.org

* Based on public data released from the European Southern Observatory VLTI obtained from the ESO/ST-ECF Science Archive Facility. The VLTI was operated with the commissioning instrument VINCI and the MONA beam combiner.

trasts. Consequently, direct interferometric limb-darkening observations of stars with compact atmospheres, i.e. visibility measurements in the 2nd lobe, have so far been limited to a small number of stars (including Hanbury Brown et al. 1974; Di Benedetto & Foy 1986; Quirrenbach et al. 1996; Burns et al. 1997; Hajian et al. 1998; Wittkowski et al. 2001). For stars with extended atmospheres, described by for instance Gaussian-type or two-component-type CLVs, measurements of high to medium spatial frequencies of the 1st lobe of the visibility function may lead to CLV constraints as well (see, e.g. Haniff et al. 1995; Perrin et al. 1999). Furthermore, lunar occultation measurements may also enable a reconstruction of the CLV (e.g. Richichi et al. 1990). Recent optical multi-wavelength measurements of the cool giants γ Sge and BY Boo (Wittkowski et al. 2001) succeeded not only in directly detecting the limb-darkening effect, but also in constraining ATLAS 9 (Kurucz 1993) model atmosphere parameters. Aufdenberg & Hauschildt (2003) showed that these γ Sge interferometric measurements and γ Sge spectroscopic measurements both compare well with predictions by the same spherical PHOENIX model atmosphere (Hauschildt et al. 1999).

Here, we present limb-darkening observations of the M4 giant star ψ Phe (HD 11695, HR 555, FK5 67, HIP 8837), obtained during the commissioning period of the ESO Very Large Telescope Interferometer (VLTI) with its commissioning instrument VINCI. VINCI is operated with one near-infrared K -band filter and could not provide measurements at different spectral bands. Spectrally resolved VLTI measurements are planned with the upcoming instruments AMBER (Petrov et al. 2003) for near-infrared wavelengths, and MIDI (Leinert et al. 2003) for mid-infrared wavelengths. We construct a spherical hydrostatic PHOENIX model atmosphere based on spectrophotometric data from the literature. This is the usual procedure to obtain a model atmosphere since additional interferometric observations are usually not available. This resulting atmosphere model predicts the LD intensity profile, a prediction that we confront with our interferometric measurement in order to test it. Agreement of the model prediction and our measurement increases confidence in atmosphere modeling for cool giants. In addition, we compare predictions of a plane-parallel PHOENIX model atmosphere as well as of standard plane-parallel ATLAS 9 (Kurucz 1993) and ATLAS 12 (Kurucz 1996, 2003) atmosphere models.

The observations and methods presented here are also a precursor for more detailed limb-darkening measurements and observations of other stellar surface features. The feasibility to derive stellar surface structure parameters beyond diameters and limb-darkening using VLTI and its scientific instruments has been studied by, e.g., von der Lühse (1997), Jankov et al. (2001), and Wittkowski et al. (2002).

2. Characteristics of ψ Phe

2.1. ψ Phe – A spectroscopic binary ?

The Hipparcos Catalogue (Perryman & ESA 1997) notes in the spectral type column that ψ Phe is a spectroscopic binary (“M4III SB”). ψ Phe is hardly worthy of the spectroscopic

binary designation. There is no mention of this star in the “Catalogue of the orbital elements of spectroscopic binary systems” (Batten et al. 1989). Likely sources for the “SB” note are Houk (1978) and Wilson (1953). The radial velocity from Wilson (1953) is noted with a (poor) grade “c” and the designation “SB”. The “SB” appears to be based on a note by Lunt (1919): “either obviously variable in velocity or suspected”. Since then, a small number of radial velocity measurements (Evans et al. 1957; Jones 1972; Crampton & Evans 1973; Jones & Fischer 1984) have failed to show variations in ψ Phe’s radial velocity.

While the variability of ψ Phe’s radial velocity has not been convincingly established, it is clear that ψ Phe is a small-amplitude ($\Delta V = \pm 0.1$), short-period (≈ 30 d), photometric variable star (Eggen 1973). Our high spatial frequency observations (see Sect. 4.1) cover two days or $\sim 1/15$ of the photometric period. We are not able to establish the photometric phase of the interferometric observations since there was no follow-up to Eggen’s original photometry.

2.2. The bolometric flux of ψ Phe

We determine the bolometric flux of ψ Phe to be $F_{\text{Bol}} = (3.2 \pm 0.3) \times 10^{-9} \text{ W m}^{-2}$, derived from a spline fit and integration of the available spectrophotometry. We have used the narrow-band spectrophotometric data ($\Delta\lambda = 2.5 \text{ nm}$, 400 nm – 700 nm) from Burnashev (1985) and the medium- and broad-band optical/near-IR photometric data from Johnson & Mitchell (1975, 1977) and Feast et al. (1990). The absolute calibration of the 13-color photometry is taken from Johnson & Mitchell (1975, 1977). The absolute calibration of JKLM photometry is from Johnson (1965) while the H-band calibration is from Bessel & Brett (1988). We have assumed a uniform 5% error for all absolute fluxes. The color excess towards ψ Phe is very low due its high galactic latitude ($b = -67^\circ$). The COBE dust maps (Schlegel et al. 1998) indicate that the *maximum* $E(B - V)$ value for this line-of-sight is 0.026 and we take this as the upper limit on $E(B - V)$. This uncertainty in the interstellar extinction is included in the derived bolometric flux. The V -band variability of ψ Phe, which we have not included, may be a source of additional uncertainty in F_{bol} .

2.3. A priori estimate of fundamental parameters

In order to decide on the grid of ψ Phe’s mass, radius, and effective temperature to explore, we roughly estimate these parameters. The diameter of ψ Phe has never been measured before by a direct technique. Using the calibration of Dyck et al. (1996), based on the spectral type and the K -magnitude, we derive a Rosseland angular diameter of $8.0 \pm 0.8 \text{ mas}$. Here, the Rosseland radius is defined as the radius at which the Rosseland optical depth equals unity, a definition that we follow in this article.

With our value for F_{bol} , T_{eff} is constrained to $3500 \pm 260 \text{ K}$. With the Hipparcos parallax, the linear Rosseland radius is derived to $85 \pm 10 R_{\odot}$, and the luminosity to $\log L/L_{\odot} = 2.99 \pm 0.23$. With these values we can place ψ Phe on the theoretical

Table 1. Properties of ψ Phe. The upper table lists the adopted literature values (visual-infrared K -band magnitude, spectral type, metallicity, parallax, bolometric flux). The lower table compares the Rosseland angular diameter and the effective temperature with their 1σ errors as derived in this work using different methods, as well as derived parameters (effective temperature, Rosseland radius, luminosity, mass, surface gravity) with their errors.

	V	K	Sp. Type	$[Z/Z_{\odot}]$	π	F_{bol}	
ψ Phe	4.3-4.5 (period ≈ 30 d) ¹	-0.63 ± 0.02 ²	M4 III ³	0.25 ± 0.1 ⁴	10.15 ± 0.15 mas ⁵	$(3.2 \pm 0.3) \times 10^{-9}$ W m ⁻² ⁶	
	¹ Eggen (1973); ² Gezari et al. (1999); ³ Houk (1978); ⁴ Feast et al. (1990); ⁵ Perryman & ESA (1997); ⁶ see Sect. 2.2						
	Photometric estimates	Fit of spherical PHOENIX model to spectrophotometry	spherical PHOENIX	plane-parallel PHOENIX model to our interferometric data	plane-parallel ATLAS 9	plane-parallel ATLAS 12	Final values
	Sect. 2.3	Sect. 3.2	Sect. 5	Sect. 5	Sect. 5	Sect. 5	Sect. 6
θ_{Ross} (mas)	8.0 ± 0.8 ^a	8.0 ± 0.4	8.13 ± 0.2	8.17 ± 0.2	8.24 ± 0.2	8.19 ± 0.2	8.13 ± 0.2 ^g
T_{eff} (K)		3550 ± 50					3550 ± 50 ^h
T_{eff} (K)	3500 ± 260 ^b	3500 ± 170 ^b					3472 ± 125 ^b
R/R_{\odot}	85 ± 10 ^c	85 ± 6 ^c					86 ± 3 ^c
$\log L/L_{\odot}$	2.99 ± 0.23 ^d	3.01 ± 0.08 ^d					3.02 ± 0.06 ^d
M/M_{\odot}	$1.2^{+0.8}_{-0.6}$ ^e	1.2 ± 0.4 ^e					1.3 ± 0.2 ^e
$\log g$ (cgs)	$0.66^{+0.33}_{-0.57}$ ^f	$0.66^{+0.18}_{-0.23}$ ^f					$0.68^{+0.10}_{-0.11}$ ^f

^a Using the calibration by Dyck et al. (1996) based on the spectral type and the K -magnitude; ^b With θ_{Ross} and F_{bol} ; ^c with θ_{Ross} and π ; ^d with R and T_{eff} ; ^e with L , T_{eff} , and the evolutionary tracks by Girardi et al. (2000), see Fig. 1; ^f with M and R ; ^g from spherical PHOENIX model fit to interferometric data, ^h from spherical PHOENIX model fit to spectrophotometry.

H-R diagram (see Fig. 1). Together with the evolutionary tracks of Girardi et al. (2000), these values for T_{eff} and L give a mass estimate of $1.2^{+0.8}_{-0.6} M_{\odot}$, and a $\log g$ estimate of $0.66^{+0.33}_{-0.57}$. Feast et al. (1990) derive a metallicity $[Z/Z_{\odot}]$ of 0.25 ± 0.08 , based on JHK photometry and atmosphere models by Bessell et al. (1989). However, they argue that this offset might be an artifact since $[Z/Z_{\odot}] = 0$ should be appropriate for local M giants. The values given in this section are summarized in Table 1.

3. Calculation of atmosphere models for ψ Phe

The modeling of atmospheres of cool giant stars, such as ψ Phe, is complicated by two effects, the treatment of molecular opacities (molecules form due to the low temperatures), and the effects of their spherical extension (cf. Plez et al. 1992; Hauschildt et al. 1999). The appropriateness of using a plane-parallel model is based on the photospheric scale height relative to the radius of the star. For the sun, with a photospheric thickness of ~ 1000 km, the extension of the photosphere relative to the solar radius is $\sim 0.1\%$. For ψ Phe the predicted photospheric thickness is $\sim 4,000,000$ km and with a radius of $\sim 85 R_{\odot}$, the extension is $\sim 6\%$. Atmosphere models for M giants including spherical extension effects have been discussed by, e.g., Scholz & Tsuji (1984); Scholz (1985); Bessell et al. (1989, 1991); Plez et al. (1992); Hofmann & Scholz (1998); and Hauschildt et al. (1999). Here, we employ hydrostatic spherically symmetric PHOENIX models including state-of-the-art treatment of molecular opacities. These models are based on the PHOENIX/NextGen models by Hauschildt et al. (1999). We compare our observational results as well to a hydrostatic plane-parallel PHOENIX model. Tabulated model CLVs based on hydrostatic plane-parallel ATLAS 9 models are publicly

available (Kurucz 1993) and often used for the interpretation of interferometric measurements of different stars including cool giants. These models are also used to parametrize LD profiles (for instance, Claret 2000, 2003; Davis et al. 2000). We compare the predictions by these standard models as well. Finally, we use a hydrostatic plane-parallel ATLAS 12 model (Kurucz 1996, 2003) which, compared to the ATLAS 9 models, includes an improved treatment of the molecular opacities, but no spherical extension effects.

3.1. PHOENIX model atmospheres

We have computed new, fully line-blanketed (7×10^5 atomic lines and 9×10^7 molecular lines), spherical, hydrostatic atmosphere models with solar photospheric abundances (Grevesse & Noels 1993) with version 13 of the PHOENIX code (for a general description see Hauschildt & Baron 1999). The three most important input parameters for our spherical models are the effective temperature, the surface gravity, and the stellar mass. Our new models start from the NextGen model grid of Hauschildt et al. (1999) with a stellar mass of $0.5 M_{\odot}$. The microturbulence for all our new models is 2 km s^{-1} , as adopted for the NextGen grid. The new model structures are iteratively converged with temperature corrections following energy conservation for convective and radiative equilibrium. We have computed a grid of 63 new models at seven temperatures: 3450, 3475, 3500, 3525, 3550, 3575, 3600 K; three gravities: 0.5, 0.7, 1.0; and three masses 0.7, 1.0, $1.3 M_{\odot}$. In addition we have computed 27 models at masses 2.0, 2.5, $3.0 M_{\odot}$ for temperatures 3500, 3550, 3600 K and gravities 0.5, 0.7, 1.0 in order to study the effect of higher masses; as well as 7 additional models at gravities 0.0, 0.25, 0.5, 0.7, 1.0, 1.25, 1.5 for

mass $1.0 M_{\odot}$ and temperature 3550 K in order to study the effects of different gravities over a larger range. For each model, we tabulate the intensity profile at 64 angles for wavelengths from $1.8 \mu\text{m}$ to $2.5 \mu\text{m}$ in steps of 0.5 nm. The mass and input surface gravity fix the reference radius (at $\tau(\text{Rosseland})=1$) at which the effective temperature is defined. Furthermore, the mass effectively regulates the relative extension of the atmosphere for fixed values of the effective temperature and gravity. In hydrostatic equilibrium, the thickness of the atmosphere relative to the overall radius increases as the mass decreases. One way to quantify the relative extension or degree of compactness of a hydrostatic stellar atmosphere is to compare the gas-pressure scale height with the stellar radius (see Bessell et al. 1991; Baschek et al. 1991). In extended atmospheres the pressure scale height is a significant fraction of the stellar radius, thus the ratio of these quantities is a useful quantity. For a fixed gravity, the stellar mass does not directly affect the pressure scale height, $H_p = \frac{RT}{\mu g_{\text{eff}}}$, where R is the gas constant, T is the temperature, μ is the mean molecular weight, and g_{eff} is the effective gravity which includes radiative and turbulent acceleration terms. On the other hand, the stellar mass does directly affect the stellar radius, $R = \sqrt{GM/g}$, where G is the gravitational constant, M is the stellar mass, and g is the gravity. Hence the ratio H_p/R decreases with increasing mass for a fixed value of gravity. Therefore, in the hydrostatic context, spherical atmospheres for massive stars are more compact than for lower mass stars with the same effective temperature and gravity. As a result the mass can affect synthetic limb intensity profiles and therefore can be an important parameter when comparing spherical model atmosphere predictions to interferometric data. Angular diameter, temperature, gravity, and mass are, of course, dependent parameters and can not be independently explored over large ranges.

For comparison, we use as well a hydrostatic plane-parallel PHOENIX model with an effective temperature of 3550 K and $\log g = 0.7$. The intensity profile is tabulated at 64 angles for wavelengths from $1.8 \mu\text{m}$ to $2.5 \mu\text{m}$ in steps of 0.5 nm, as for the spherical models.

3.2. Comparison of PHOENIX models with spectrophotometry

The effective temperature and angular diameter of ψ Phe can be constrained by comparing synthetic spectral energy distributions (SEDs) from the spherical PHOENIX models with the observed spectrophotometry. To do so, synthetic photometry is performed using the 13-color filter sensitivity functions from Johnson & Mitchell (1975) compiled by Moro & Munari (2000) and the JHKLM filter sensitivity functions from Bessell & Brett (1988). The synthetic spectrophotometry values are scaled to the observed values by the factor

$$\frac{1}{4} \theta_{\text{Ross}}^2 10^{-0.4 \frac{A_{\lambda}}{A_V} R_V E(B-V)}$$

where θ_{Ross} is the wavelength-independent Rosseland angular diameter, A_{λ}/A_V is the extinction curve relative to the V-band, $E(B-V)$ is the color excess, and we assume $R_V = 3.1 = A_V/E(B-V)$ using the extinction curves of Cardelli et al. (1989)

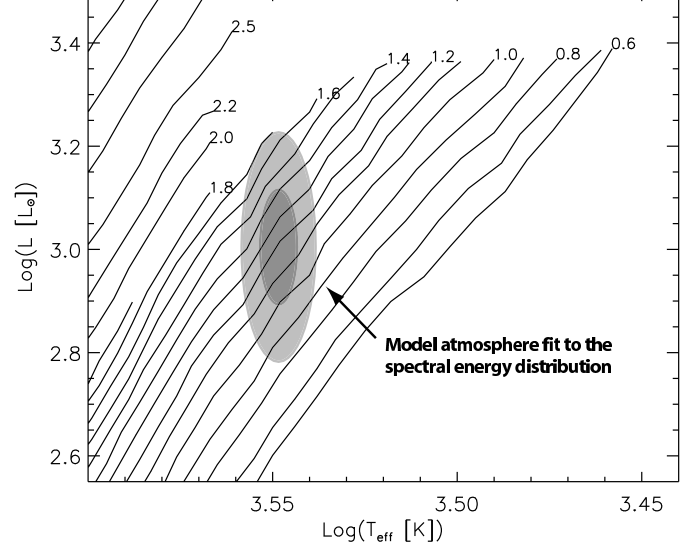


Fig. 1. The predicted regions for ψ Phe in the Hertzsprung-Russell diagram from the model atmosphere fitting to the observed spectral energy distribution. The method provides values for T_{eff} and θ_{Ross} , and together with the parallax, a luminosity. The error ellipses show 1- and 2-sigma zones. Also shown are the evolutionary tracks of Girardi et al. (2000) for masses $M > 0.6 M_{\odot}$.

A comparison of the best fit synthetic SED to the 13-color photometry, which covers the widest wavelength range contemporaneously, with all the spectrophotometric data is shown in Fig. 2. The shape of the near-infrared continuum and the strong TiO bands in the optical provide the principal constraints on T_{eff} , while the fluxes in absolute units constrain θ_{Ross} . The best fit parameters, based on least-squares fits to the photometry and application of the F-test (Aufdenberg et al. 2002) are $T_{\text{eff}} = 3550 \pm 50$ K and $\theta_{\text{Ross}} = 8.0 \pm 0.4$ mas. Together with the parallax (Table 1), the ranges in these values translate into the 1- and 2-sigma uncertainty regions on the theoretical HR diagram in Fig. 1. The uncertainty in the luminosity is somewhat of an overestimate, since the best fit values for T_{eff} and θ_{Ross} are not independent.

While T_{eff} and θ_{Ross} are well constrained by the SED fit alone, the surface gravity and mass are not. However, relying on the evolutionary tracks from Girardi (2000), the 2-sigma region on the HR diagram indicates that the mass is $1.2 \pm 0.4 M_{\odot}$. A surface gravity then follows from this mass, θ_{Ross} , and the parallax: $\log g = 0.66^{+0.18}_{-0.23}$. Since these constraints are much tighter than can be derived from comparisons to spectrophotometry alone, the mass and surface gravity parameters for the synthetic spectrum shown in Fig. 2 were chosen to be consistent with these values. Table 1 gives a summary of the derived values.

3.3. ATLAS model atmospheres

In addition to the PHOENIX models, we employ intensity profiles predicted by standard plane-parallel hydrostatic ATLAS 9 model atmospheres from the Kurucz CD-ROMS (Kurucz

HR 555 = ψ Phe M4 III

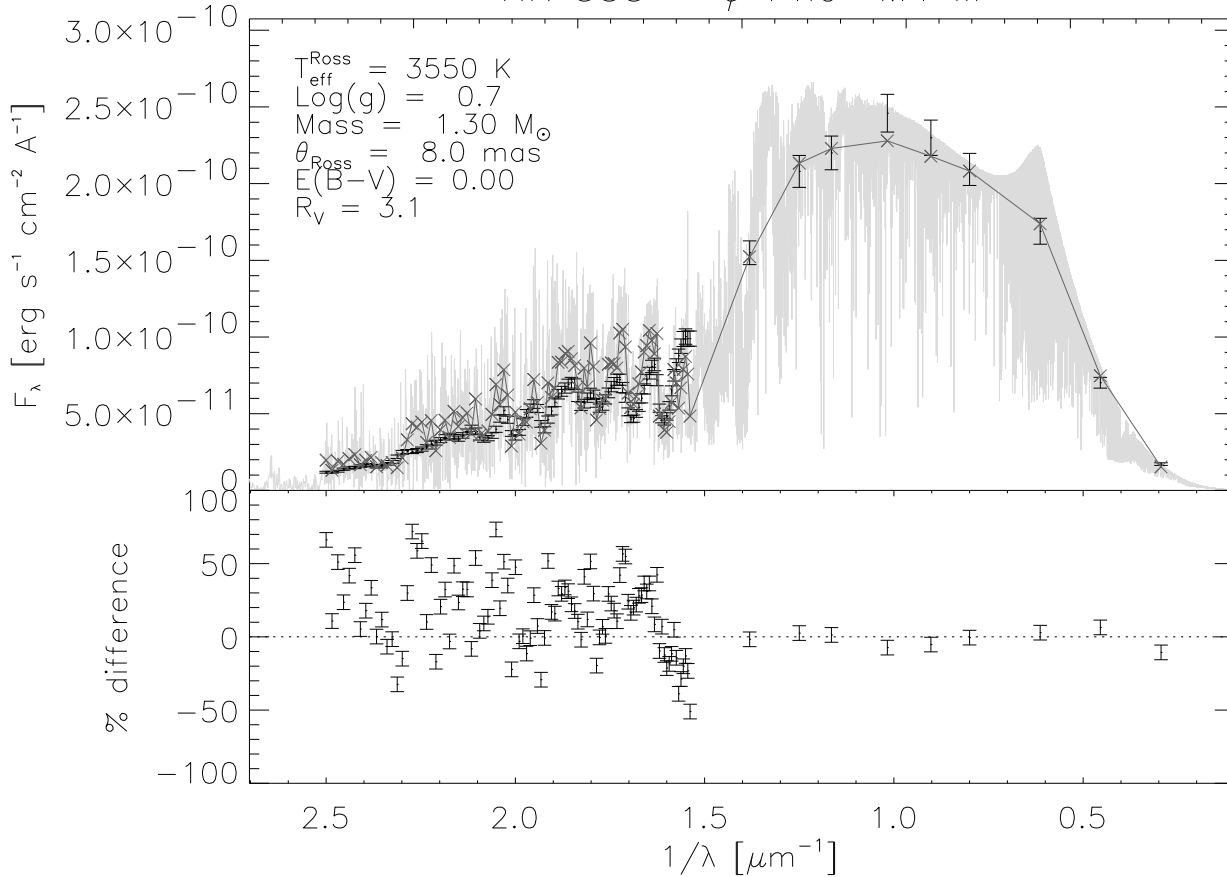


Fig. 2. (Top) Spectral energy distribution of ψ Phe (error bars) compared with synthetic photometry ('x's) for the narrow and broad-band photometry derived from a high-resolution model spectrum (spherical PHOENIX model) shown in gray. (Bottom) The percentage difference between the observed and synthetic photometry in each wavelength bin. The model parameters are derived by a least-squares fit to only the 13-color photometry (Johnson & Mitchell 1975), while this Fig. shows the model comparison to all available data, as described in the text.

1993). The Kurucz CDROMs tabulate monochromatic LD profiles for 17 angles in 1221 frequency intervals ranging from 9.09 nm to 160 000 nm. In the range of the near-infrared K -band filter (1800–2500 nm), the frequencies are sampled in steps of 10 nm. This data is available for different chemical abundances, microturbulent velocities, effective temperatures and surface gravities. To be consistent, we have chosen the parameters to be closest to those determined for our favorite PHOENIX model, i.e. the model that best fits the spectrophotometry (Sect. 3.2). These parameter values are T_{eff} 3500 and 3750 K, $\log g$ 0.5 and 1.0, solar chemical abundance, and a standard microturbulent velocity of 2 km sec^{-1} (file kurucz.cfa.harvard.edu/grids/gridP00/ip00k2.pck19).

Finally, we employ a plane-parallel hydrostatic ATLAS 12 model which includes an improved treatment of the opacities (Kurucz 1996, 2003). We have chosen again the parameters of our favorite spherical PHOENIX model for reasons of consistency, i.e. $T_{\text{eff}} = 3550 \text{ K}$, $\log g = 0.7$, and solar chemical abun-

dance. The ATLAS 12 intensity profile is tabulated at 16 angles for wavelengths from $1.8 \mu\text{m}$ to $2.5 \mu\text{m}$ in steps of 0.5 nm.

3.4. Effects of model geometry on the interpretation of fitted angular diameters

We use spherical PHOENIX models as well as plane-parallel PHOENIX and ATLAS models, as described above, for the fits to our interferometric data. The fit result for both geometries is the LD diameter θ_{LD} at which the intensity reaches zero (see Sect. 4.5 below). Figure 3 illustrates CLV predictions by spherical and plane-parallel PHOENIX models ($T_{\text{eff}} = 3550 \text{ K}$, $\log g = 0.7$, mass of the spherical model $1.3 M_\odot$; CLVs are calculated for the broad VINCI K passband). The monochromatic contributions over the K -band to this passband-averaged spherical CLV are shown below in Fig. 5 (middle). It illustrates that our broad-band measurement is dominated by continuum K -band photons, and that it has only little line contamination (relative to a strong molecular band). The escaping continuum

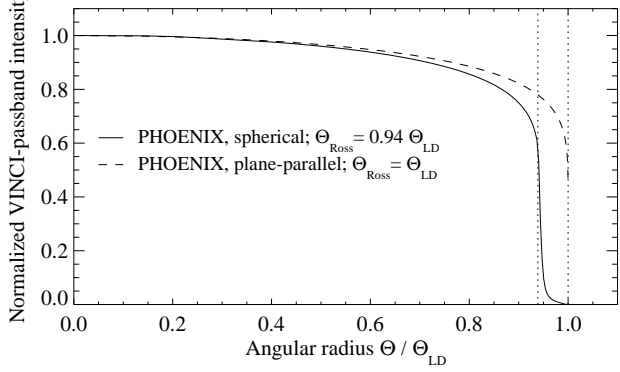


Fig. 3. Comparison of CLVs predicted by a spherical (solid lines) and a plane-parallel (dashed lines) PHOENIX model, both with the same 0% intensity diameter θ_{LD} . Both models have parameters $T_{\text{eff}}=3550$ K, $\log g=0.7$. The spherical model has a mass of $1.3 M_{\odot}$. Both CLVs are computed for the broad-band VINCI sensitivity function (K -band). The two CLVs differ by a tail-like extension for the spherical model which is missing for the plane-parallel model. We describe the diameters of both models by the Rosseland diameter, which is close to the point where the CLV drops steeply and most continuum photons escape. The θ_{Ross} values for these two model geometries differ by a factor of 0.94, while the θ_{LD} values correspond.

photons originate from a rather compact zone at $\mu \sim 0.3$. The spherical CLV shows an inflection point and a tail-like extension which is caused by the optically-thin limb of the spherical model. The plane-parallel model is semi-infinite for all angles θ and has a singularity at $\theta = 90^\circ$ or $\theta = \theta_{LD}$. This causes the sharp edge of the plane-parallel CLV and its lack of any tail-like extension. As a result, despite the correspondence of the θ_{LD} values, the points where the CLVs drop steeply, which is also the point where most continuum photons escape, do not correspond for these two model geometries. In other words, different θ_{LD} fit values are expected for plane-parallel and spherical model geometries using the same physical data. We use the Rosseland diameter θ_{Ross} , which is associated with a Rosseland optical depth of unity, to describe the stellar diameters. The Rosseland diameter is close to the compact zone where most continuum photons escape and where the CLV drops steeply, and is hence comparable for both model geometries.

For the plane-parallel models, we assume $\theta_{LD} \equiv \theta_{\text{Ross}}$, since the plane-parallel CLVs drop steeply to zero directly at the stellar limb.

For the spherical models, θ_{LD} is associated with the outermost shell of the model (at R_0) and the wavelength-independent conversion factor from θ_{LD} to θ_{Ross} is the ratio $C_{\text{Ross/LD}} = R(\tau_{\text{Ross}} = 1)/R_0$. Here, the outermost radius R_0 of the model is defined by the standard outer boundary conditions for our model atmospheres, which are a continuum optical depth of $1e-6$ at $1.2 \mu\text{m}$ and an outer gas pressure of $1e-4$ dynes/cm². The inner optical depth boundary is 100 at $1.2 \mu\text{m}$. The radial grid and outermost radius differ from model to model, resulting in a model-dependent conversion factor $C_{\text{Ross/LD}}$ (as used in Table 5, Sect. 5 below).

4. VLTI/VINCI measurements

4.1. Observations

The ESO VLTI, located on Cerro Paranal in northern Chile, is currently in the phase of commissioning. For a recent general overview see Glindemann et al. (2003) and references therein. First fringes using 40 cm test siderostats and the commissioning instrument VINCI (Kervella et al. 2003a) were achieved in March 2001, followed by first fringes using the 8.2 m diameter Unit Telescopes (UTs) on October 30, 2001. First fringes with the first scientific instrument, the mid-infrared instrument MIDI (Leinert et al. 2003), were obtained in December 2002.

Our observations of ψ Phe’s squared visibility amplitudes beyond the first minimum employing the UTs succeeded one month after the achievement of first fringes with the UTs, and were first mentioned in ESO press release 23/01 (Nov. 5, 2001). These visibility values of ψ Phe were obtained during the nights starting on Nov. 1 & 2, 2001 using the UT 1 – UT 3 102 m baseline of the VLTI, and the VINCI instrument, as part of the VLTI commissioning. The UTs were not yet equipped with adaptive optics nor a tip-tilt corrector. High-contrast fringes at short spatial frequencies were obtained before and after the UT measurements using the 40 cm test siderostats. These data, as all scientifically interesting VLTI/VINCI data, have been made publicly available through the ESO archive. Table 2 details our observations and Table 3 shows the adopted properties of the used calibration stars.

The use of the large apertures of the 8 m UTs together with the use of single-mode optical fibers, a technique that is known to lead to very accurate visibility measurements (see, e.g. Coudé du Foresto 1998), has enabled precise measurements of low visibility amplitudes. Bootstrapping techniques, such as those used by Hajian et al. (1998) and Wittkowski et al. (2001) to detect and track fringes with weak contrasts, were not necessary.

Configurations using different aperture sizes for different baseline lengths, as used here, might be an interesting perspective for the completed VLTI as well. The completed VLTI will routinely allow the measurement of the limb-darkening effect for many stars, and open the possibility to obtain stellar surface structure parameters beyond limb-darkening (see e.g., Wittkowski et al. 2002). This will require visibility data uniformly distributed over the uv -plane including both, high-contrast fringes in the first lobe as well as very low-contrast fringes in the second and following lobes of the visibility function. Then, the lowest fringe contrasts can be measured with the 8 m UTs in order to obtain a sufficient signal-to-noise ratio (S/N) for fringe detection and tracking and/or an enhanced S/N for these important low visibility points while higher fringe contrasts on the same source can be obtained with the 1.8 m ATs.

Our data were recorded through the VINCI K -band filter. The scan length of the optical path difference was $280 \mu\text{m}$, the fringe frequency, i.e. the time needed to scan one interferometric fringe, was 296 Hz for the siderostat data and 695 Hz for the UT data. Our data were taken as series of 100 or 500 interferogram scans.

Table 2. Record of our ψ Phe observations. Listed are the date of observation, the used stations, the baseline length, the number of series of interferograms, and the used calibration stars.

Date	Stations	B (m)	#	Calibration stars
2001-10-12	E0/G0	16	4	β Cet, ϵ Lep
2001-10-16	E0/G0	16	3	β Cet, η Cet
2001-10-17	E0/G0	16	3	β Cet, η Cet
2001-10-18	E0/G0	16	3	β Cet, η Cet
2001-11-01	UT 1/UT 3	102	13	χ Phe, γ^2 Vol
2001-11-02	UT 1/UT 3	102	5	39 Eri, γ^2 Vol
2001-11-04	E0/G0	16	7	β Cet, ϵ Lep
2001-11-05	E0/G0	16	3	β Cet, ϵ Lep

Table 3. Properties of the used calibration stars. Listed are the spectral type from Perryman & ESA (1997), the K -band magnitude from Gezari (1999), the effective temperature T_{eff} derived from the spectral type, the effective wavelength λ_0 derived from T_{eff} and the VINCI sensitivity curve, the adopted K -band UD diameter and its error $e\theta$. The sources for the adopted diameter values and their errors are (1) Cohen et al. (1999) and/or (2) Bordé et al. (2002).

Obj.	SpT	K	T_{eff} K	λ_{eff} μm	θ_{UD}^K mas	$e\theta$ mas	Ref.
β Cet	K0III	-0.2	4800	2.179	5.18	0.06	1,2
ϵ Lep	K4III	-0.2	4075	2.181	5.91	0.06	1,2
η Cet	K2III	0.9	4600	2.180	3.35	0.04	1,2
χ Phe	K5III	1.5	4000	2.181	2.69	0.03	1,2
γ^2 Vol	K0III	1.5 ^a	4800	2.179	2.44	0.06	1
39 Eri	K3III	2.3	4200	2.181	1.81	0.02	1

^a from V and the $V - K$ color for a K0 III star.

4.2. Data reduction

We have used a modified version (Kervella et al. 2003b) of the standard VINCI data reduction pipeline (Ballester et al. 2002), whose general principle is based on the original algorithm of the FLUOR instrument (Coudé du Foresto et al. 1997; Coudé du Foresto et al. 1998). This data reduction software includes the following procedures.

For each scan, the two interferograms produced from the two interferometric outputs of the VINCI beam combiner are calibrated for photometric intensity fluctuations using the two photometric outputs. After this first photometric calibration, the two calibrated interferograms are subtracted to remove residual photometric fluctuations. Since the two fringe patterns are in perfect phase opposition, this subtraction removes a large part of the correlated fluctuations while enhancing the interferometric fringes. This is particularly important for the small ψ Phe visibility amplitudes in the second lobe of the visibility function obtained with the UT1-UT3 baseline. Instead of the classical Fourier analysis, the time-frequency analysis (Ségransan et al. 1999) based on the continuous wavelet transform (Farge 1992) is used to derive the wavelet power spectral density (wavelet PSD) of each scan. The differential piston corrupts the amplitude and the shape of the fringe peak in the PSD. A selection of single scans is used to remove interferograms that are affected by strong differential piston and, if existent,

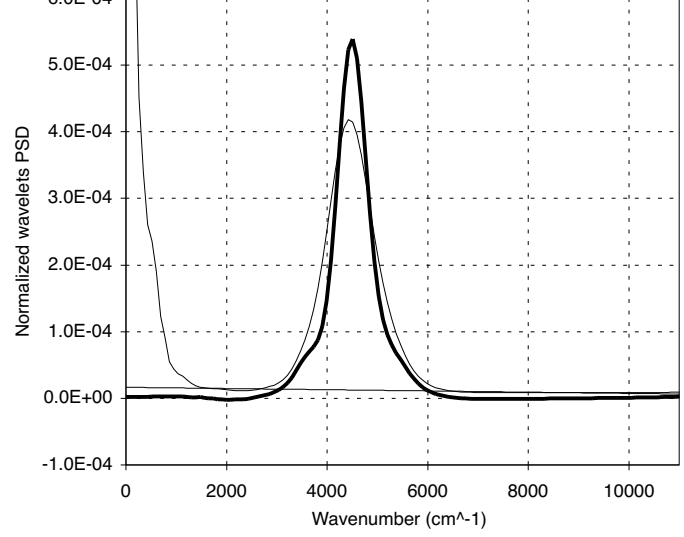


Fig. 4. Average wavelets PSD of one series (Date 2001-11-02, Univ. Time 05:23:23) of 414 accepted interferograms obtained on ψ Phe (UT1-UT3 baseline). The thin curve is the simple average of all PSD before removal of the background. The background is estimated by a fit of a linear function to low and high frequency PSD values outside the fringe signal (ranges [1400..2000] cm^{-1} and [8000..9988] cm^{-1}) and compensated. The squared coherence factor is derived from the integration of the background calibrated PSD (thick line) in the range [2000..8000] cm^{-1} . Before averaging, each fringe peak is re-centered to the theoretical frequency of the fringes in order to reduce the energy spreading due to the differential piston effect before the power peak integration. This is the reason why the shape of the non-re-centered (thin line) and re-centered and bias corrected (thick line) PSDs are not exactly the same.

that show no fringes. The selection criteria include checks of the peak width in the time domain ($\pm 50\%$ around theoretical value is accepted), as well as the peak position ($\pm 30\%$ around theoretical value is accepted) and peak width in the frequency domain ($\pm 40\%$ around theoretical value is accepted). In addition, fringe scans with low photometric signal (S/N of less than 5), with a large jump of the optical path difference before the scan (larger than $20\mu\text{m}$), and with fringes at the edge of the scan are rejected. The average wavelet PSD of the selected interferograms is computed.

The use of squared quantities, such as the PSD, requires attention to a possible additive background of the PSD caused by residual photon and detection noise, despite the first compensations mentioned above. The relative contribution of remaining biases would be highest for small visibility values, such as those studied here (cf. Wittkowski et al. 2001). In the case of the VINCI data reduction, the residual noise background is determined from a least squares fit to low and high frequency PSD values outside the fringe signal, and compensated. Figure 4 shows an example of the average wavelet PSD derived from one series of 414 accepted interferograms obtained on ψ Phe using UT1 and UT3. Shown are the raw PSD before compensation of the residual PSD background, the derived model of the PSD background, and the compensated PSD. Despite the very

strong photometric fluctuations that are observed in the multi-speckle regime, and despite the very low fringe signal (for this particular PSD, the squared visibility amplitude of ψ Phe was only $|V|^2 = 0.013$), the background calibrated wavelet PSD is free of any photometric contamination. This is very important to reliably obtain our small ψ Phe squared visibility values beyond the first minimum.

The coherence factor values are finally derived by integrating the compensated average wavelet PSD of the selected interferograms. This integration includes fringe power at all wavelengths over the broad VINCI sensitivity band. Single scans with coherence factors that differ by more than 3σ from the median of the sample are rejected.

4.3. Calibration

Table 2 lists the calibration stars that have been used during the different nights of our ψ Phe observations; Table 3 details their characteristics including the adopted diameters and their errors.

Owing to the low limiting magnitude of the siderostats ($K_{\text{corr}} \simeq 1$ at the time of these observations), the calibration stars for the 16 m siderostat baseline have diameters, between 3 mas and 6 mas, which are not small compared to the expected ψ Phe diameter of $\simeq 8$ mas. Thus, the calibration requires special attention to the adopted diameter values. Cohen et al. (1999) have used a spectro-photometric calibration to derive high-precision Rosseland diameters and their errors for a list of 422 sources. They found that their estimates compare well with several other diameter estimates. This was confirmed by Bordé et al. (2002), who in addition reduced this list to 374 stars carefully selected to be used as calibration stars for long baseline stellar interferometry. We rely on these diameter estimates and their errors as given in the lists by Cohen et al. (1999) and Bordé et al. (2002). The main calibration star for the siderostat data, β Cet, used during all siderostat nights, was in August 2002 calibrated against the Cohen stars 20 Cet (M0 III, $\theta_{\text{UD}}^K = 3.41 \pm 0.037$ mas) and ι Cet (K1 III, $\theta_{\text{UD}}^K = 3.27 \pm 0.036$ mas) using the 64 m G1–E0 baseline. The measured β Cet diameter was found to be well consistent with the Cohen value and its error given in Table 3. An additional calibration uncertainty arises from the fact that the 16 m baseline measurements, corresponding to squared visibility amplitudes in the range ~ 0.8 – 0.95 , only marginally resolve our object ψ Phe. To take these calibration uncertainties for the 16 m baseline into account, we weight the measurements obtained with this baselines by a factor of two lower than the 102 m baseline measurements. A VLTI program in order to derive calibration star diameters in a self-consistent way from VLTI observations is in progress (Percheron et al. 2003).

For the ψ Phe data sets as well as all calibration star data sets, the coherence factors c^2 are computed as described in Sect. 4.2. The transfer function t^2 is computed for all calibration star data sets as $t^2 = c^2/|V|^2$, where $|V|^2$ is the adopted squared visibility amplitude for the respective time and baseline using the adopted diameter value and effective wavelength from Table 3. The transfer function value for the time of each of the ψ Phe observations is then obtained as a weighted av-

erage of the calibration stars' t^2 values during the night with the weight being a product of (1) a Gaussian function of the time difference from the respective ψ Phe measurement with a width σ of 3 hours for the siderostat data and 2 hours for the UT data, and (2) the error of the single transfer function measurement consisting of the statistical c^2 error and the error resulting from the adopted diameter uncertainty. The final ψ Phe squared visibility values are then obtained by division of the ψ Phe coherence factors by the transfer function values obtained for the respective time. The final errors of the ψ Phe squared visibility amplitudes are computed from the error of the ψ Phe coherence factor (the scatter of the single scan's coherence factors) and the uncertainty of the transfer function values, which include the errors of the calibration stars' coherence factors, the adopted diameter errors, and the variation of the computed transfer function over the night.

4.4. Results

Table 4 shows the resulting squared visibility amplitudes $|V|^2$ for each of our data sets. The given errors of $|V|^2$ include the statistical error obtained from the scatter of the single scan values, the uncertainty of the calibration star's diameter (see Table 3), and the variation of the computed transfer function over the night (see Sect. 4.3). A plot (Figure 6) of our measured $|V|^2$ values together with best fitting PHOENIX and ATLAS models is discussed in Sect. 5 (below).

4.5. Computation of broad-band model visibility values

The use of the VINCI broad-band K filter influences the obtained squared visibility amplitudes in two ways (cf. Tango & Davis 2002). Firstly, the stellar intensity profile is not observed at a monochromatic wavelength λ but integrated over the broad-band sensitivity curve. The strength of the limb-darkening effect for ψ Phe, is expected to vary over the VINCI sensitivity curve. Figure 5 shows the expected variation of ψ Phe's flux, intensity profile, and strength of the limb-darkening (correction factors from LD to UD diameters) over the VINCI passband. The VINCI passband-averaged intensity profile and strength of the limb-darkening are shown as well. The plots show that our K -band measurements are dominated by continuum photons and that there is only little line contamination (relative to a strong molecular band). Secondly, squared visibility amplitudes are averaged over different spatial frequencies ($B/[(\lambda_0 - \Delta\lambda) \dots (\lambda_0 + \Delta\lambda)]$) for any point of observation with fixed baseline B and a broad-band filter (central wavelength λ_0 , filter width $\Delta\lambda$). This latter effect has been discussed by Kervella et al. (2003b) for the VINCI instrument and been referred to as "bandwidth smearing".

The calculation of the synthetic broad-band squared visibility amplitudes has to follow the way the measured squared visibility amplitudes are derived from the raw fringe data. For the VINCI data reduction (see Sect. 4.2), first the PSD, a squared quantity corresponding to the squared visibility amplitudes, is computed from the interferograms, and then the coherence factor is derived from the integral of the PSD, which includes

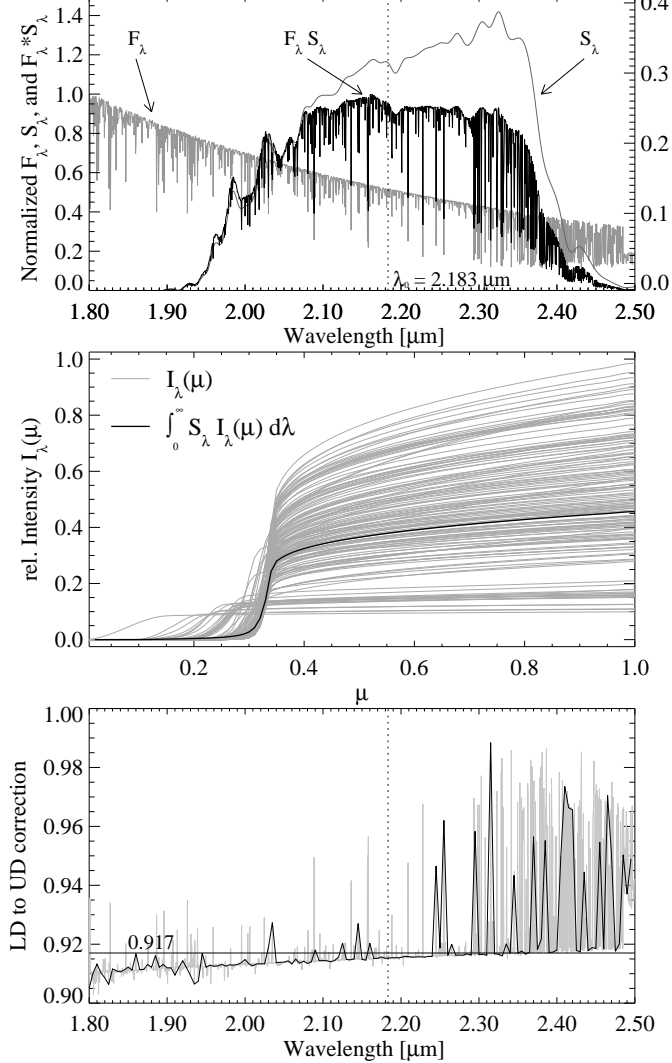


Fig. 5. (Top) Model ψ Phe K -band spectrum F_λ (gray), VINCI sensitivity function S_λ (gray; right scale), and effective spectrum $F_\lambda S_\lambda$ (black). The dashed vertical line denotes the effective wavelength $\lambda_0 = 2.183 \mu\text{m}$. (Middle) Monochromatic model ψ Phe intensity profiles across the K -band with a resolution of 50 nm (gray) and their S_λ weighted average (calculated with 5 nm resolution, black). With VLTI and AMBER, it will in principle be possible to directly measure these different intensity profiles with a resolution of up to ~ 0.2 nm. (Bottom) Monochromatic correction factors from LD to UD diameters with a resolution of 5 nm (gray) and 50 nm (black) between $1.8 \mu\text{m}$ and $2.5 \mu\text{m}$. The horizontal line denotes the weighted average of the correction factors (value 0.917). The spherical PHOENIX model as used in Fig. 2 was employed for these plots. The spectrum shows CO lines at the red end, which have a significant impact on the ψ Phe intensity profiles at *these* wavelengths. They become optically thin near the limb and hence, the limb is less dark, the radius is larger in the bands, and the LD-to-UD correction factor is closer to unity. At most wavelengths the limb edge is at $\mu \sim 0.3$, but at a minority of wavelengths the limb is brighter, almost uniform at one wavelength. These profiles come from wavelengths in the CO band. These CO lines, however, do not have a strong influence on the VINCI passband-averaged model intensity profile because of their narrowness, their lower intensity, and the shape of S_λ . The LD-to-UD correction factors show also the general trend that the (continuum) intensity profiles become closer to a uniform disk with increasing wavelength.

Table 4. Resulting visibility amplitudes $|V|^2$ for each series of interferograms. Given are the date, the Universal Time, the spatial frequency B/λ_0 ($1''$) for ψ Phe's effective wavelength of $\lambda_0 = 2.183 \mu\text{m}$, the squared visibility amplitudes, their error $\sigma(|V|^2)$, and the number (#) of accepted scans.

Date	Univ. Time	B/λ_0 ($1''$)	$ V ^2$	σ	#
2001-10-13	03:40:05	35.29	8.471e-01	4.902e-02	462
10-13	04:24:29	35.55	8.580e-01	5.038e-02	439
10-13	04:59:41	35.39	8.084e-01	4.938e-02	460
10-13	05:41:03	34.74	8.306e-01	5.054e-02	452
10-17	01:56:26	33.82	8.805e-01	2.306e-02	479
10-17	04:48:29	35.34	8.721e-01	2.650e-02	450
10-17	06:13:42	33.29	8.739e-01	2.742e-02	483
10-18	01:54:08	33.86	8.666e-01	2.082e-02	463
10-18	03:12:03	35.20	8.409e-01	2.270e-02	395
10-18	04:35:33	35.43	8.626e-01	2.442e-02	433
10-19	03:02:01	35.12	8.694e-01	1.754e-02	444
10-19	04:09:31	35.54	8.668e-01	1.712e-02	481
10-19	05:25:09	34.55	8.625e-01	1.739e-02	464
11-02	05:17:37	201.09	1.196e-02	7.545e-04	50
11-02	05:20:05	200.53	1.318e-02	7.164e-04	398
11-02	05:23:23	199.76	1.317e-02	7.220e-04	414
11-02	05:25:21	199.30	1.325e-02	7.388e-04	62
11-02	05:27:49	198.70	1.318e-02	7.309e-04	413
11-02	05:31:00	197.93	1.317e-02	7.371e-04	411
11-02	05:34:13	197.13	1.317e-02	7.425e-04	433
11-02	06:20:40	183.95	9.144e-03	7.091e-04	66
11-02	06:32:42	180.01	8.605e-03	7.322e-04	77
11-02	06:35:13	179.16	8.391e-03	7.009e-04	308
11-02	06:38:38	178.00	8.000e-03	6.891e-04	329
11-02	06:42:02	176.82	7.847e-03	6.887e-04	286
11-03	02:50:05	221.37	1.266e-02	1.385e-03	81
11-03	02:52:31	221.20	1.197e-02	1.360e-03	387
11-03	02:55:47	220.96	1.180e-02	1.369e-03	354
11-03	02:58:52	220.72	1.221e-02	1.410e-03	386
11-03	03:02:10	220.46	1.223e-02	1.430e-03	426
11-05	04:56:32	33.37	8.622e-01	2.822e-02	348
11-05	05:06:35	32.98	8.767e-01	2.458e-02	492
11-05	05:11:46	32.77	8.804e-01	2.466e-02	492
11-05	06:13:25	29.69	8.832e-01	2.218e-02	195
11-05	06:25:05	29.00	9.048e-01	2.592e-02	413
11-05	06:35:29	28.36	9.159e-01	2.572e-02	453
11-05	07:53:25	23.19	9.643e-01	2.640e-02	427
11-06	01:41:53	35.00	8.640e-01	2.294e-02	454
11-06	01:46:19	35.06	8.598e-01	2.312e-02	484
11-06	01:50:41	35.12	8.612e-01	2.336e-02	479

fringe power from all wavelengths over the sensitivity band. Hence, for VINCI, the model squared visibility amplitudes at different wavelengths and spatial frequencies have to be integrated (see Kervella et al. 2003b), and not the complex visibilities (visibility amplitudes with sign) as implied by the general formalism in Tango & Davis (2002). This means that the broadband squared visibility amplitude values never reach zero in our case.

We derive non-normalized monochromatic LD model visibility values $V_{LD}(\lambda)$ on a grid of wavelengths (range $1.8..2.5 \mu\text{m}$ in steps of 0.5 nm for our PHOENIX models) by numerical evaluation of the Hankel transform of the intensity profiles I_λ^μ tab-

ulated for each of these (1400) monochromatic wavelengths λ (following Davis et al. 2000 and Tango & Davis 2002, see also the use in Wittkowski et al. 2001) by

$$V_{\text{LD}}(\lambda) = \int_0^1 S_\lambda I_\lambda^\mu J_0[\pi \theta_{\text{LD}} (B/\lambda) (1 - \mu^2)^{1/2}] \mu d\mu \quad (1)$$

Here, I_λ^μ is used as a function of μ , $\mu = \cos \theta$ ($\mu \in [0, 1]$, $\mu=0$ corresponds to the star's radius at which the intensity reaches zero, and $\mu=1$ to the star's center); S_λ is the VINCI instrument's sensitivity curve including the transmissions of the atmosphere, the optical fibers, the VINCI K -band filter, and the detector quantum efficiency; B is the sky-projected baseline length. For reasons of numerical accuracy, it had been necessary to interpolate the tabulated intensity profiles onto a regularly sampled grid of μ values (we have chosen a cubic-spline interpolation onto 100 μ values), rather than interpolating the more complex argument of the integral in Eq. 1. The integral is then computed using a 5-point Newton-Cotes algorithm. We have checked the accuracy of the algorithm by comparing results for tabulated UD and FDD intensity profiles with their available analytic expressions for V . In order to calculate a spatial frequency B/λ_0 , as used in Fig. 6 (below), an effective wavelength λ_0 is computed as

$$\lambda_0 = \frac{\int_0^\infty S_\lambda F_\lambda \lambda d\lambda}{\int_0^\infty S_\lambda F_\lambda d\lambda} \quad (2)$$

with F_λ being the stellar flux at wavelength λ :

$$F_\lambda = \int_0^1 I_\lambda(\mu) \mu d\mu. \quad (3)$$

With our favorite spherical PHOENIX model for ψ Phe as derived in Sect. 3.2, Fig. 2, we obtain $\lambda_0 = 2.183 \mu\text{m}$. This value characterizes the wavelength of our measurement, but is not used for the calculation of the synthetic visibilities since they are calculated for the full wavelength range in Eq. 1. The functions S_λ and F_λ , as well as the effective wavelength are shown in Fig. 5 (top). As for the processing of the instrument data, each monochromatic visibility is not normalized separately. The VINCI passband-averaged squared visibility amplitudes are finally computed as

$$|V_{\text{LD}}|^2 = \frac{\int_0^\infty |V_{\text{LD}}(\lambda)|^2 d\lambda}{\int_0^\infty S_\lambda^2 F_\lambda^2 d\lambda}, \quad (4)$$

including the proper normalization by the total detected flux.

We directly use the model atmosphere's tabulated intensity profiles (the stellar radiation field) in Eq. 1. No approximation of the intensity profile by any limb-darkening law is used. This ensures two important points: Parametrizations of intensity profiles are usually very good approximations for the visibility curve before the first minimum, but may lead to deviations from the original visibility profile beyond the first minimum, which may be significant with the precision of our measurement. Furthermore, the direct use of the tabulated model stellar radiation field on a fine grid of wavelengths enables us to compute the model squared visibility values for exactly our

instrument's passband, while published limb-darkening coefficients are calculated for specific filter curves which do not well resemble the VINCI sensitivity curve including e.g. the transmission of the optical fibers and the detector efficiency.

As discussed in Sect. 3.4, the LD diameter used in Eq. 1 depends on the detailed model structure and is therefore not a well suited quantity for reference. We transform θ_{LD} into the Rosseland angular diameter θ_{Ross} with the factor $C_{\text{Ross/LD}}$ defined in Sect. 3.4.

5. Comparison of our VLT/VINCI data to our model predictions

We use the different model atmospheres as described in Sect. 3 and, with the formalism described above in Sect. 4.5, calculate synthetic squared visibility amplitudes for the spatial frequencies of our data. For each considered model, we find by a non-linear least squares fit the θ_{LD} value for which the synthetic and measured squared visibility amplitudes have the lowest χ^2 value. The LD angular diameter θ_{LD} is treated as the only free parameter. The best fitting θ_{LD} value is then transformed into the Rosseland angular diameter θ_{Ross} using the factors $C_{\text{Ross/LD}}$ defined in Sect. 3.4.

Table 5 lists the fit results for the different spherical PHOENIX, and plane-parallel PHOENIX, ATLAS 12, and ATLAS 9 models. The first three columns specify the model parameters T_{eff} , $\log g$, and M , followed by the model-specific factor $C_{\text{Ross/LD}}$. The next two columns give the best fitting θ_{LD} values together with the reduced χ_v^2 values. Finally, the results for θ_{Ross} are given in the last column. The formal errors for θ_{LD} are found to be about uniform for all considered models. The standard formal error $\sigma(\theta_{\text{LD}})$ for θ_{LD} , derived as the $\Delta\theta_{\text{LD}}$ corresponding to $\Delta\chi^2 = 1$, is ~ 0.05 mas. Deriving the error by means of the F -test, which is a more reliable estimate than the χ^2 -test (e.g., Bevington & Robinson 1992), we obtain $\sigma(\theta_{\text{LD}}) \sim 0.12$ mas. Here, we assume a number of degrees of freedom of 39, i.e. the number of visibility points minus one. The real situation is more complicated because (1) the errors include statistical errors as well as systematic errors (which can not easily be separated), (2) some squared visibility value measurements are not independent but linked via the same calibration measurements, (3) the visibility function is sampled at two different spatial frequency regions using different telescopes, and (4) obtained χ_v^2 values are larger than unity. We estimate the final error $\sigma(\theta_{\text{LD}})$, including calibration uncertainties, to be ~ 0.2 mas by comparing results obtained by different calibrations and different sub-samples of our data. Table 5 shows results for our favorite model atmosphere from Sect. 3.2, i.e. the spherical PHOENIX model with $T_{\text{eff}}=3550$ K, $\log g=0.7$, and $M=1.3M_\odot$. In addition, we consider spherical PHOENIX models with varied parameters that are still consistent with the estimates in Sect. 3.2. Furthermore, we compare plane-parallel PHOENIX, ATLAS 12, and ATLAS 9 models with, for reasons of consistency, parameters closest to our favorite model.

Figure 6 plots our measured squared visibility values together with the model prediction by our favorite spherical PHOENIX model with best fitting θ_{LD} value. Shown are also the predictions by corresponding plane-parallel PHOENIX,

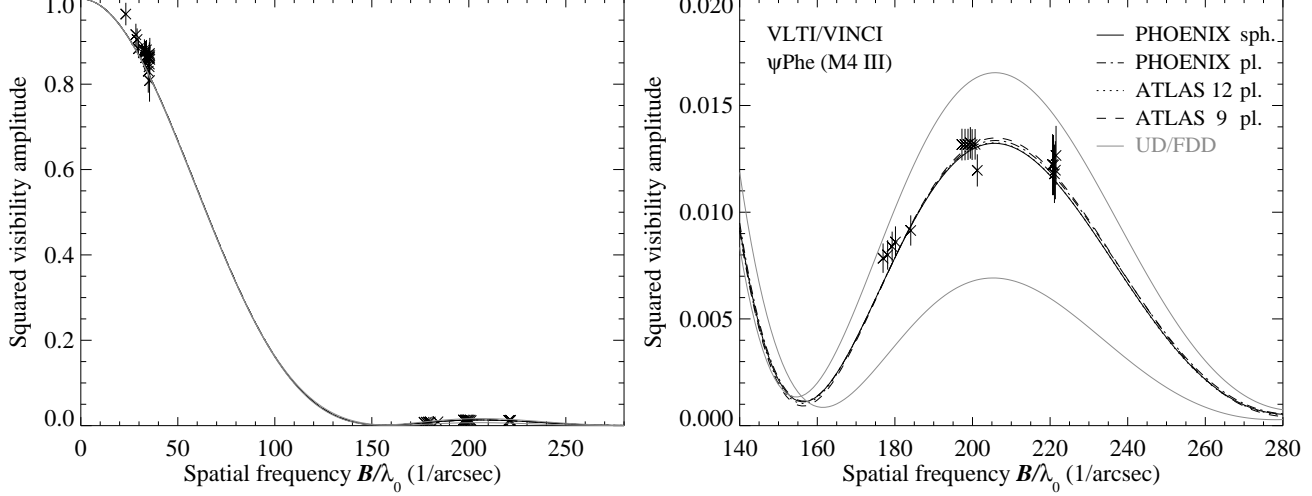


Fig. 6. Our measured squared visibility amplitudes of ψ Phe ('x' symbols with error bars) together with the (solid black line) spherical PHOENIX model prediction with model parameters T_{eff} , $\log g$, and mass as derived from spectrophotometry and model evolutionary tracks (Sect. 3.2), and best fitting θ_{LD} value. Shown are also the (dashed-dotted line) plane-parallel PHOENIX model, (dotted line) plane-parallel ATLAS 12 model, (dashed line) plane-parallel ATLAS 9 model, all with corresponding model parameters and best fitting θ_{LD} . As a reference for the strength of the limb-darkening, the gray lines denote corresponding UD (upper line) and FDD (lower line) model visibility functions. The left panel shows the full range of the visibility function while the right panel is an enlargement of the low squared visibility amplitudes in the second lobe. All considered PHOENIX and ATLAS model predictions result in a very similar shape of the visibility function in the 2nd lobe. Our measurements are significantly different from uniform disk and fully-darkened disk models, and consistent with all considered PHOENIX and ATLAS models.

Table 5. Results for θ_{LD} obtained by fits to our interferometric data. Listed are the model input parameters T_{eff} , $\log g$, and mass M , the model-specific correction factors $C_{\text{Ross/LD}}$, the fit results for θ_{LD} , their corresponding reduced χ^2_{ν} values, and finally the Rosseland angular diameter θ_{Ross} . The error $\sigma(\theta_{\text{LD}})$ is estimated to be uniformly ± 0.2 mas for all model fits (see text).

T_{eff}	$\log g$	M	$C_{\text{Ross/LD}}$	θ_{LD}	χ^2_{ν}	θ_{Ross}
Spherical PHOENIX models:						
3550	0.7	1.3	0.9388	8.664	1.80	8.13
3500	0.7	1.3	0.9394	8.663	1.81	8.14
3600	0.7	1.3	0.9381	8.665	1.79	8.13
3550	0.5	1.3	0.9218	8.814	1.79	8.12
3550	1.0	1.3	0.9577	8.504	1.79	8.14
3550	0.7	1.0	0.9302	8.739	1.80	8.13
Plane-parallel PHOENIX model:						
3550	0.7	/	1	8.168	1.72	8.17
Plane-parallel ATLAS 12 model:						
3550	0.7	/	1	8.191	1.78	8.19
Plane-parallel ATLAS 9 models:						
3500	0.5	/	1	8.244	1.74	8.24
3500	1.0	/	1	8.243	1.73	8.24
3750	0.5	/	1	8.227	1.71	8.23
3750	1.0	/	1	8.228	1.71	8.23

ATLAS 12, and ATLAS 9 models. As a reference of the strength of the limb-darkening, UD ($I = 1$ for $0 \leq \mu \leq 1$ and $I = 0$ oth-

erwise) and FDD ($I = \mu$) model visibility functions are shown, with diameters θ_{UD} and θ_{FDD} corresponding to our favorite PHOENIX model fit. Our measurements differ significantly from UD and FDD models, confirming the limb-darkening effect. All considered PHOENIX and ATLAS model CLV predictions lead to very similar model visibility functions up to the 2nd lobe, which are all consistent with our data. Hence, our data confirm the model-predicted strength of the limb-darkening effect. Our measured values in the second lobe of the visibility function seem to lie systematically above the model predictions by ~ 0.5 - 1σ . It is not yet clear if these small differences are caused by systematic effects of our data calibration or by the model structures. The squared visibility amplitudes derived from the siderostat data show a systematic offset of about 1σ towards larger values with respect to our best fitting curves. This is likely caused by possible small systematic calibration effects, since the calibration of our high squared visibility amplitudes in the range ~ 0.8 - 0.95 derived from the siderostat data was difficult (see Sect. 4.3).

The best fitting Rosseland angular diameters are well constrained by our measurement. The measurements in the 2nd lobe of the visibility function also constrain the positions of the 1st minimum and 2nd maximum of the visibility function, which is a constraint of the diameter. This constraint is independent of possible small systematic calibration uncertainties of the $|V|^2$ values. The reduced χ^2_{ν} values for the different considered models do not show significant differences, which is consistent with the very similar predicted shapes of the model visibility functions. These similarities are expected since our measurement is dominated by continuum photons, and the

continuum forming region of the atmosphere is almost compact (see Fig. 5).

6. Discussion and conclusions

Spherical PHOENIX models We have constructed a spherical hydrostatic PHOENIX model atmosphere for ψ Phe in Sect. 3.2. Here, we confront this model’s prediction for the CLV by comparing it with our VLTI/VINCI measurement of the visibility function in the second lobe. We find that the model predicted shape of the visibility function is consistent with our VLTI/VINCI measurements. Simultaneously, the Rosseland angular diameter derived from the model and spectrophotometry $\theta_{\text{Ross}}^{\text{Spectr.}} = 8.0 \pm 0.4$ mas agrees well with the Rosseland angular diameter derived from the same model and our VLTI/VINCI measurements $\theta_{\text{Ross}}^{\text{VINCI}} = 8.13 \pm 0.2$ mas. These findings increase confidence in theoretical atmosphere modeling of cool giant (M III) stars.

Spherical PHOENIX models with varied model parameters (T_{eff} , $\log g$, M) that are still consistent with the values derived from spectrophotometry in Sect. 3.2 lead to the same best fitting values for θ_{Ross} and χ^2_{ν} . Hence, these model parameters cannot be further constrained by the shape of our measured visibility function up to the 2nd lobe beyond the constraints provided by the available spectrophotometry.

The corresponding θ_{LD} and θ_{Ross} values for these different spherical models illustrate that θ_{LD} depends on the detailed model structure and that θ_{Ross} is better suited to characterize the stellar diameter. The best fitting θ_{LD} values for the different considered spherical PHOENIX models differ by up to 0.24 mas or $\sim 3\%$, while the θ_{Ross} values for the same models differ by only up to 0.02 mas or $\sim 0.2\%$.

Plane-parallel PHOENIX and ATLAS models Our plane-parallel PHOENIX and ATLAS models with the same model parameters as used for the spherical model lead, as expected for a continuum-dominated measurement, to a very similar shape of the visibility function. These small differences can not be detected by our VLTI/VINCI measurements.

The obtained Rosseland angular diameters derived by the plane-parallel models, which we assume to equal θ_{LD} , are consistent within our error-bars with the result obtained by our favorite spherical model. However, there are systematic differences of the obtained diameter values of up to ~ 0.1 mas or $\sim 1.5\%$ as compared to the result obtained by our favourite spherical model. These differences can be explained by the different model geometries, line lists, opacity sampling techniques, and spectral resolutions of the employed models.

Final parameter values for ψ Phe Because of the 6% extension of ψ Phe’s atmosphere, we consider our favorite spherical PHOENIX model the most reliable one. However, this can currently not be verified by our VLTI/VINCI measurements. The diameter $\theta_{\text{Ross}} = 8.13 \pm 0.2$ mas derived from this model and our interferometric data is the tightest available constraint on ψ Phe’s diameter. From this angular diameter and our bolometric flux from Sect. 2.2, an effective temperature of $T_{\text{eff}} = 3472 \pm$

125 K is derived. This means that the tightest constraint on ψ Phe’s effective temperature comes from the model comparison with the available spectrophotometry in Sect. 3.2, which is $T_{\text{eff}} = 3550 \pm 50$ K. With these values ($\theta_{\text{Ross}} = 8.13 \pm 0.2$ mas, $T_{\text{eff}} = 3550 \pm 50$ K) and the Hipparcos parallax, we derive a linear Rosseland radius of $R = 86 \pm 3 R_{\odot}$ and a luminosity of $\log L/L_{\odot} = 3.02 \pm 0.06$. Together with the evolutionary tracks by Girardi et al. (2000), see Sect. 2.3 & Fig. 1, these values are consistent with a mass of $M = 1.3 \pm 0.2 M_{\odot}$ and a surface gravity of $\log g = 0.68^{+0.10}_{-0.11}$. These values are summarized in the last Col. of Table 1. They are consistent with the values derived by the different methods mentioned in earlier Sects. It would be an interesting further test to confirm the derived surface gravity and mass by means of a high-resolution spectrum.

Future measurements Our VLTI/VINCI measurements could only probe the LD intensity profile of ψ Phe averaged over the broad VINCI sensitivity band, and confirm the model-predicted strength of the limb-darkening. We have shown in Fig. 5 that the intensity profile and the strength of the limb-darkening effect of ψ Phe are expected to vary over our instrumental bandpass, especially in narrow molecular bands. While we take this predicted variation into account for the computation of the synthetic broad-band squared visibility amplitudes, it would be a better test of the model atmospheres to obtain spectrally resolved observations. Promising observations to better constrain atmospheres of cool giants would likely be direct limb-darkening measurements, i.e. observations with more than one resolution element across the stellar disk as used here, but at a number of well-defined narrow molecular and continuum bands with high spectral resolution. Theoretical studies seem to be needed and are planned to derive which observations in terms of wavelength bands and fundamental parameters of the target stars are best suited to constrain model parameters such as the model geometry and the treatment of molecular opacities. The required spectrally resolved limb-darkening observations can in the future be obtained with the upcoming scientific VLTI instruments AMBER and MIDI. AMBER will allow us to probe the stellar intensity profile with a spatial resolution λ/B of up to ~ 1 mas and with a spectral resolution $\lambda/\Delta\lambda$ of up to 10 000. AMBER can combine the light from three telescopes simultaneously, and hence obtain closure phases and triple amplitudes. The use of closure phases will likely enable the detection of additional surface features such as spots (Wittkowski et al. 2002). The use of the 1.8 m diameter ATs and the 8.2 m diameter UTs equipped with adaptive optics will allow us to obtain these measurements with a high signal-to-noise ratio.

7. Summary

We have obtained VLTI/VINCI limb-darkening measurements of ψ Phe by probing the visibility function in the 2nd lobe. Our data confirm the strength of the limb-darkening effect as well as the Rosseland angular diameter as predicted by our favorite spherical PHOENIX model atmosphere, the parameters for which were constrained by comparison to available spec-

trophometry and theoretical stellar evolution tracks. This increases confidence in stellar atmosphere modeling of cool giant (M III) stars.

We have derived high-precision fundamental parameters for ψ Phe, as listed in the last Col. of Table 1.

The measurements presented here are also a precursor for planned more detailed spectrally resolved limb-darkening measurements of a wider range of stars aiming at further constraining the effects of model geometry and the treatment of atomic and molecular lines. Observations with the completed VLTI and its scientific instruments will enable these advanced studies of stellar atmospheres.

Acknowledgements. Observations with the VLTI are only made possible through the efforts of the whole VLTI team. We thank especially the VLTI commissioning team including the Telescope Instrument Operators for the operation of the interferometer. We would like to thank the entire PHOENIX model atmosphere team, in particular Peter Hauschildt and France Allard for helpful discussions. We thank Robert L. Kurucz for making his model atmosphere data publicly available, for providing us with a new ATLAS 12 model for our source ψ Phe, and for helpful discussions. We thank T. Szeifert for valuable comments and discussions on this project. We are grateful for the valuable comments by the referee M. Scholz which helped to improve this article. This research has made use of the SIMBAD database, operated at CDS, Strasbourg, France.

References

Aufdenberg, J. P., Hauschildt, P. H., Baron, E., et al. 2002, ApJ 570, 344
Aufdenberg, J. P., & Hauschildt, P. H. 2003, Proc. SPIE 4838, 193
Ballester, P., Chavan, A. M., Glindemann, A., et al. 2002, Proc. SPIE 4844, 300
Baschek, B., Scholz, M., & Wehrse, R. 1991, A&A 246, 374
Batten, A. H., Fletcher, J. M., & MacCarthy, D. G. 1989, Publications of the Dominion Astrophysical Observatory, 17, 1
di Benedetto, G. P., & Foy, R. 1986, A&A 166, 204
Bessell, M. S., & Brett, J. M. 1988, PASP 100, 1134
Bessell, M. S., Brett, J. M., Scholz, M., Wood, P. R. 1989, A&AS 77, 1 (erratum A&AS 87, 621)
Bessell, M. S., Brett, J. M., Scholz, M., Wood, P. R. 1991, A&AS 89, 335
Bevington, P. R., & Robinson, D. K. 1992, Data Reduction and Error Analysis for the Physical Sciences (WCB/MGraw-Hill), ISBN 0-07-911243-9
Bordé, P. J., Coudé du Foresto, V., Chagnon, G., Perrin, G. 2002, A&A 393, 183
Burnashev, V. I. 1985, Abastumanskaya Astrofiz. Obs., Byull., 59, 83
Burns, D., Baldwin, J. E., Boysen, R. C., et al. 1997, MNRAS 290, L11
Cardelli, J. A., Clayton, G. C., & Mathis J. S. 1989, ApJ 345, 245
Claret, A. 2000, A&A 363, 1081
Claret, A. 2003, A&A 401, 657
Cohen, M., Walker, R. G., Carter, B., et al. 1999, AJ 117, 1864
Coudé du Foresto, V., Ridgway, S., Mariotti, J.-M. 1997, A&AS 121, 379
Coudé du Foresto, V., Perrin, G., Ruilier, C., et al. 1998, Proc. SPIE 3350, 856
Coudé du Foresto, V. 1998, ASP Conf. Series, 152, 309
Crampton, D., & Evans, L. T. 1973, MNRAS 162, 11
Davis, J., Tango, W. J., & Booth, A. J. 2000, MNRAS 318, 387

Dyck, H. M., Benson, J. A., van Belle, G. T., Ridgway, S. T. 1996, AJ 111, 1705
Eggen, O. J. 1973, ApJ 184, 793
Evans, D. S., Menzies, A., & Stoy, R. H. 1957, MNRAS 117, 534
Farge, M., 1992, Annual Review of Fluid Mechanics 24, 395
Feast, M. W., Whitelock, P. A., & Carter, B. S., 1990, MNRAS 247, 227
Gezari, D. Y., Pitts, P. S., & Schmitz, M. 1999 Catalog of Infrared Observations, Edition 5 (Gezari+ 1999), VizieR On-line Data Catalog: II/225.
Girardi, L., Bressan, A., Bertelli, G., Chiosi, C. 2000, A&AS 141, 371
Glindemann, A., et al. 2003, Proc. SPIE 4838, 89
Grevesse, N., & Noels, A., 1993, in Origin and Evolution of the Elements, eds. N. Pranto, E. Vangioni-Flam & M. Casse, Cambridge: Cambridge Univ. Press, 14
Hajian, A. R., Armstrong, J. T., Hummel, C. A., et al. 1998, ApJ 496, 484
Hanbury Brown, R., Davis, J., Lake, R. J. W., Thompson, R.J. 1974, MNRAS 167, 475
Haniff, C. A., Scholz, M., & Tuthill, P. G. 1995, MNRAS 276, 640
Hauschildt, P. H., & Baron, E., 1999, J. Comp. Appl. Math 109, 41
Hauschildt, P. H., Allard, F., Ferguson, J., Baron, E., Alexander, D. R. 1999, ApJ 525, 871
Hofmann, K.-H., & Scholz, M. 1998, A&A 335, 637
Houk, N. 1978, Michigan catalogue of two-dimensional spectral types for the HD stars, Vol. 2 (Ann Arbor: Department of Astronomy, University of Michigan)
Jankov, S., Vakili, F., Dominiciano de Souza, A., Janot-Pacheco, E. 2001., A&A 377, 721
Johnson, H. J. 1965, Comm. Lunar Plan. Lab. 3, 73
Johnson, H. L., & Mitchell, R. I. 1975, RMxAA 1, 299
Johnson, H. L., & Mitchell, R. I. 1977, RMxAA 2, 269
Jones, D. H. P. 1972, ApJ 178, 467
Jones, D. H. P., & Fisher, J. L. 1984, A&AS 56, 449
Kervella, P., Gitton, P., Ségransan, D., et al. 2003, Proc. SPIE 4838, 858
Kervella, P., Ségransan, D., & Coudé du Foresto, V. 2003, in preparation
Kurucz, R. 1993, Limbdarkening for 2 km/s grid (No. 13): [+0.0] to [-5.0]. Kurucz CD-ROM No. 17. Cambridge, Mass.: Smithsonian Astrophysical Observatory, 1993
Kurucz, R. 1996, ASP Conf. Ser. 108, 160
Kurucz, R. 2003, private communication
Leinert, C., Graser, U., Waters, L., et al. 2003, Proc. SPIE 4838, 893
Lunt, J. 1919, ApJ 50, 161
Moro, D., & Munari, U. 2000, A&AS 147, 361
Percheron, I., Richichi, A., & Wittkowski, M. 2003, Proc. SPIE 4838, 1424
Perrin G., Coudé du Foresto, V., Ridgway, S. T., et al. 1999, A&A 345, 221
Perryman, M. A. C., ESA 1997, The HIPPARCOS and TYCHO catalogues, ESA SP Series vol. 1200, Noordwijk, Netherlands: ESA Publications Division
Petrov, R. G., Malbet, F., Weigelt, G., et al. 2003, Proc. SPIE 4838, 924
Plez, B., Brett, J.M., & Nordlund, A. 1992, A&A 256, 551
Quirrenbach, A., Mozurkewich, D., Buscher, D. F., Hummel, C. A., Armstrong, J.T. 1996, A&A 312, 160
Richichi, A., Lisi, F. 1990, A&A 230, 355
Schlegel, D. J., Finkbeiner, D. P., & Davis M. 1998, ApJ 500, 525
Scholz, M. 1985, A&A 145, 251
Scholz, M. 2001, MNRAS 321, 347
Scholz, M., & Takeda, Y. 1987, A&A 186, 200

- Scholz, M., & Tsuji, T. 1984, A&A 130, 11
- Ségransan, D., Forveille, T., Millan-Gabet, C. P. R., Traub, W. A. 1999, ASP Conf. Ser. 194, 290
- Tango, W. J., & Davis, J. 2002, MNRAS 333, 642
- von der Lühе, O. 1997, in “Science with the VLT Interferometer” (Springer: Berlin), p. 303
- Wilson, R. E. 1953, General Catalogue of Stellar Radial Velocities (Washington, D.C.: Carnegie Institution)
- Wittkowski, M., Hummel, C. A., Johnston, K. J., et al. 2001, A&A 377, 981
- Wittkowski, M., Schöller, M., Hubrig, S., Posselt, B., von der Lühе, O. 2002, Astron. Nachr. 323, 241